GEOPHYSICS, VOL. 77, NO. 5 (SEPTEMBER-OCTOBER 2012); P. S105–S115, 14 FIGS., 2 TABLES.
10.1190/GEO2011-0455.1

An angle-domain imaging condition for elastic reverse time migration and its application to angle gather extraction

Rui Yan[1] and Xiao-Bi Xie[1]

ABSTRACT

An angle-domain imaging condition is recommended for multicomponent elastic reverse time migration. The local slant stack method is used to separate source and receiver waves into P- and S-waves and simultaneously decompose them into local plane waves along different propagation directions. We calculated the angle-domain partial images by crosscorrelating every possible combination of the incident and scattered plane P- and S-waves and then organized them into P-P and P-S local image matrices. Local image matrix preserves all the angle information related to the seismic events. Thus, by working in the image matrix, it is convenient to perform different angle-domain operations (e.g., filtering artifacts, correcting polarity, or conducting illumination and acquisition aperture compensations). Because local image matrix is localized in space, these operations can be designed to be highly flexible, e.g., target-oriented, dip-angle-dependent or reflection-angle-dependent. After performing angle-domain operations, we can stack the partial images in the local image matrix to generate the depth image, or partially sum them up to produce different angle-domain common image gathers, which can be used for amplitude versus angle and migration velocity analysis. We tested several numerical examples to demonstrate the applications of this angle-domain image condition.

INTRODUCTION

Advances in multicomponent seismic acquisition and computational capability start to shift the seismic practice from imaging with pressure waves in an acoustic fluid to imaging using elastic waves with realistic anisotropic parameters. Due to the elastic properties of earth materials, both P- and S-waves can propagate within the earth. The combinations of P- and S-wave data, rather than P-wave data alone, can yield previously unavailable information about the targets and give better constrains on the physical properties of subsurface. In addition, S-waves are also able, in some cases, to image structures that P-waves cannot adequately portray, such as those beneath the high-velocity bodies. However, more sophisticated imaging techniques are required to extract the new information from the multicomponent data. By neglecting P- and S-wave couplings during migration, some approaches separate the multicomponent data into P- and S-modes and extrapolate them independently with scalar propagators (e.g., Zhe and Greenhalgh, 1997; Sun and McMechan, 2001; Hou and Marfurt, 2002) or elastic propagators (e.g., Xie and Wu, 2005). Other approaches do not separate P- and S-modes on the surface, but extrapolate the entire multicomponent data at once. These techniques include Kirchhoff migration (e.g., Kuo and Dai, 1984; Dai and Kuo, 1986; Hokstad, 2000) and elastic reverse time migration (RTM) (e.g., Sun and McMechan, 1986; Chang and McMechan, 1987, 1994). Among the existing migration methods, elastic RTM can better preserve kinematic and dynamic features of elastic waves in complex models, and resulting seismic images more accurately characterize the subsurface. It is further explored by some authors (e.g., Yan and Sava, 2008; Lu et al., 2009; Yan and Xie, 2010).

One important issue in the elastic RTM is the imaging condition. The conventional zero-time-zero-offset crosscorrelation imaging condition (Claerbout, 1985) sums up waves coming from all directions. This will create a spatial image that effectively suppresses the noise in the data but also eliminates the directional information in the image. In contrast, expanding the image in angle domain, i.e., generating angle-domain common image gathers (ADCIGs), adds an extra dimension to the conventional image. For example, the move-out of the ADCIG carries the phase or traveltime errors for waves propagating in different angles through the velocity model. They can be used for migration velocity analysis. Dynamic information such as amplitude versus angle (AVA) is crucial in reservoir interpretation. However, complex overburden structures often obscure the signals from the reservoir. Extracting AVA from the ADCIG provides an effective way to remove the propagation effect. So imaging in the

Manuscript received by the Editor 12 November 2011; revised manuscript received 11 April 2012; published online 8 August 2012.
[1]University of California, Department of Earth and Planetary Sciences, Santa Cruz, California, USA. E-mail: rxyan@ucsc.edu; xxie@ucsc.edu.

local angle domain and imaging using elastic waves are essential elements in obtaining reliable petrophysical parameters.

ADCIGs have been extracted in Kirchhoff prestack depth migration (Xu et al., 2001; Brandsberg-Dahl et al., 2003). For wave equation based migration, several techniques have been adopted to extract the ADCIGs. In the source-receiver migration based on double square root equation (e.g., Mosher et al., 1997; Prucha et al., 1999; Mosher and Foster, 2000; Jin et al., 2002), the angle information can be obtained from the wavefield in local wavenumber domain.

For shot profile wave-equation migration, available methods fall into three categories. In the first category, ADCIGs are obtained by first decomposing source and receiver wavefields into localized beams with different directions, followed by an imaging condition applying to these localized beams around the image point. The ADCIGs can be extracted for either one-way wave equation based methods (Xie and Wu, 2002; Wu and Chen, 2003; Chen et al., 2006) or full-wave equation-based RTM (Zhang et al., 2010; and Xu et al., 2011). With this method, the angle decomposition is independent of the image process. The resulted method can be applied to angle-related analyses other than generating ADCIGs, e.g., directional illumination (e.g., Wu et al., 2003; Luo et al., 2004; Wu and Chen, 2002, 2006; Xie et al., 2006; Xie and Yang, 2008; Cao and Wu, 2009b; Mao and Wu, 2010), resolution and image amplitude compensation (e.g., Xie et al., 2005b; Wu et al., 2006; Cao and Wu, 2009a).

In the second category, ADCIGs are extracted during the imaging stage, where the extended images with space and/or time lags are first calculated. For image with space-shift, the ADCIG can be calculated from offset-CIGs through a slant stack (e.g., Rickett and Sava, 2002; Sava and Fomel, 2003; Biondi and Symes, 2004; Sava and Vasconcelos, 2011; Sava and Vlad, 2011) or a simple radial-trace transform in Fourier domain (Sava and Fomel, 2005a, 2005c). The similar procedure can be applied to time-shift image (Sava and Fomel, 2005b) but for a 3D case, a priori information on dip angle is required.

Under the third category, the Poynting vector or the polarization vector of the P-wave is used to determine the wave propagation direction. Some authors (e.g., Zhang and McMechan, 2011a, 2011b; Yoon et al., 2011) chose to calculate the source wave direction only and focused on the contributions of one or a few most energetic phases. Then, with a known reflector dipping angle and assuming mirror reflection (i.e., the reflector is locally planar), the ADCIG is calculated. Others (e.g., Dickens and Winbow, 2011) computed the energy flux directions for the source and receiver wavefields and extracted angle dependent reflectivity at the imaging point. These methods are computationally efficient and the resulted ADCIGs have good angle resolution.

In this paper, an angle decomposition method under the first category is developed and applied to the elastic RTM for ADCIG calculation. We first decompose the reconstructed elastic wavefields into local plane waves and use them to calculate the angle-domain partial images. Second, we construct the local image matrix (LIM) that is composed of all the angle-domain partial images. LIMs for point scatters and planar reflectors are analyzed. Third, we demonstrate how to apply angle-domain operations in the LIM and convert it into ADCIGs as well as the depth image. Finally, a five-layer model and the Marmousi2 model are used as examples to demonstrate the feasibility of the approach for generating ADCIGs and depth images.

WAVEFIELD RECONSTRUCTION

The implementation of elastic RTM consists of two steps: wavefield reconstruction and application of imaging condition. The first step is to reconstruct source and receiver wavefields in the subsurface using finite difference scheme. On the source-side, the wavefields are reconstructed by solving elastic wave equation with a driving source (Aki and Richards, 1980)

$$\rho \frac{\partial^2 \mathbf{u}(\mathbf{x}, t)}{\partial t^2} - \nabla \cdot \sigma(\mathbf{x}, t) = \delta(\mathbf{x} - \mathbf{x}_S)\mathbf{s}(t), \tag{1}$$

where $\mathbf{s}(t)$ is the source time function, $\mathbf{x}_S$ is the source location; $\mathbf{u}(\mathbf{x}, t)$ is the displacement wavefield, $\sigma(\mathbf{x}, t)$ is the stress tensor wavefield. In an isotropic medium, the relationship between stress and displacement is

$$\sigma = \lambda \mathbf{I} \nabla \cdot \mathbf{u} + \mu(\nabla \mathbf{u} + \mathbf{u}\nabla), \tag{2}$$

where ρ is the density, λ and μ are the Lame's constants, $\mathbf{I}$ is the identity matrix. On the receiver-side, the recorded multicomponent data are set to be the boundary condition of the elastic wave equation

$$\begin{cases} \rho \frac{\partial^2 \mathbf{u}(\mathbf{x},t)}{\partial t^2} - \nabla \cdot \sigma(\mathbf{x}, t) = 0, \\ \mathbf{u}(\mathbf{x}, t)|_B = \mathbf{u}_0(\mathbf{x}, t), \end{cases} \tag{3}$$

where $\mathbf{u}_0(\mathbf{x}, t)$ is the multicomponent seismic data recorded at the receiving surface B. Note that the above boundary condition is valid only for a plane surface. Otherwise, a complete boundary condition including displacement and stress may be required.

MODE SEPARATION AND ANGLE DECOMPOSITION

In the elastic RTM scenario, the reconstructed wavefields are vectorized and P- and S-modes are coupled. The image formed by direct crosscorrelation of source and receiver wavefields mixes the contributions from P- and S-waves and is difficult to interpret. To get the images with clear physical meaning, it is preferred to separate P- and S-modes, and implement the imaging condition as crosscorrelation of pure wave modes. In an isotropic medium, the mode separation can be achieved in space domain (Sun et al., 2001; Yan and Sava, 2008) or wavenumber domain (Dellinger and Etgen, 1990; Zhang and McMechan, 2010). The space-domain divergence and curl can separate a mixed-mode wavefield into P- and S-waves but introduce distortions in the separated wavefields (Sun et al., 2001). On the contrary, the wavenumber- or slowness-domain separation preserves the waveforms of the original wavefield. Given a propagation direction at an image location, P-wave polarization is parallel to it while S-wave polarization is perpendicular to it; P- and S-waves can be separated by projecting the displacement to the two polarization directions.

To build an angle-domain imaging condition, P- and S-modes need to be decomposed into superposition of local plane waves (or beams) propagating in various directions. Techniques such as local slant stack (Xie and Wu, 2002) and beamlet decomposition (Wu and Chen, 2002, 2003; Soubaras, 2003; Chen et al., 2006; Wu et al., 2008; Wu and Mao, 2007) have been developed for one-way wave equation based migration methods. However, they

may not lead to good results when applied to RTM. To handle the full wavefield, calculations need be performed in horizontal and vertical directions (Cao and Wu, 2009b). Time-domain local slant stack (Xie and Lay, 1994; Xie et al., 2005a; Xie and Yang, 2008; Yan and Xie, 2009, 2010) and windowed fast Fourier transform (FFT) (Zhang et al., 2010; Xu et al., 2011) have been proposed for this purpose. Here, by combining the method for one-way migration (slant stack in frequency domain) and the time-domain method (slant stack in multidimensional space), we present a slowness-based decomposition implemented simultaneously with the mode separation. We first use the Fourier transform to convert the reconstructed wavefields from time domain to frequency domain. In the frequency domain, the mixed-mode wavefield $\mathbf{u}(\mathbf{x},\omega)$ is decomposed into P- and S-components localized in space and slowness

$$\mathbf{u}^{\mathrm{P}}(\mathbf{p},\mathbf{x},\omega)=\int W(\mathbf{x}'-\mathbf{x})\hat{\mathbf{e}}\cdot[\mathbf{u}(\mathbf{x}',\omega)\cdot\hat{\mathbf{e}}]\times e^{-i\omega(\mathbf{x}'-\mathbf{x})\cdot\mathbf{p}}d\mathbf{x}', \tag{4}$$

$$\mathbf{u}^{\mathrm{S}}(\mathbf{p},\mathbf{x},\omega)=\int W(\mathbf{x}'-\mathbf{x})\hat{\mathbf{e}}\times[\mathbf{u}(\mathbf{x}',\omega)\times\hat{\mathbf{e}}]\times e^{-i\omega(\mathbf{x}'-\mathbf{x})\cdot\mathbf{p}}d\mathbf{x}', \tag{5}$$

where $\mathbf{u}^{\mathrm{P}}(\mathbf{p},\mathbf{x},\omega)$ and $\mathbf{u}^{\mathrm{S}}(\mathbf{p},\mathbf{x},\omega)$ are the P- and S-waves in local slowness domain, $W(\mathbf{x}'-\mathbf{x})$ is a window function centered at $\mathbf{x}$, $\mathbf{p}$ is the slowness vector and $\hat{\mathbf{e}}=\mathbf{p}/p$ is a unit vector toward the propagation direction, p is the absolute value of $\mathbf{p}$.

Illustrated in Figure 1 is a flowchart of slowness analysis at an image point $\mathbf{x}$ in 2D geometry. The frequency-domain wavefields are sampled by a spatial window and shown as data volumes 1a and 1b. Using equations 4 and 5, they can be transformed to slowness-frequency data volumes 1c and 1d. Shown in Figure 1e and 1f are the cross sections of data volumes 1c and 1d at the dominant frequency. They illustrate in the slowness domain the wave energy is distributed around P- and S-wave dispersion circles and each energy peak denotes a local plane wave. This indicates, to decompose the elastic wavefield into local plane waves, we do not need compute every component in the slowness domain. Rather, we only calculate along dispersion circles. In this way, the computational cost will be tremendously reduced. Thus, instead convert 1a and 1b into 1c and 1d, we calculate 1g and 1h, which are two cylindrical surfaces: the inner and outer ones are for P- and S-waves, respectively. In the 2D case, the decomposition process can be written as

$$\mathbf{u}^{\mathrm{P}}(\mathbf{x},\omega)=\sum_{\theta}\mathbf{u}^{\mathrm{P}}(\theta,\mathbf{x},\omega), \tag{6}$$

$$\mathbf{u}^{\mathrm{S}}(\mathbf{x},\omega)=\sum_{\theta}\mathbf{u}^{\mathrm{S}}(\theta,\mathbf{x},\omega), \tag{7}$$

where

$$\mathbf{u}^{\mathrm{P}}(\theta,\mathbf{x},\omega)=\omega p_{\mathrm{P}}\mathbf{u}^{\mathrm{P}}(\mathbf{p}=p_{\mathrm{P}}\hat{\mathbf{e}},\mathbf{x},\omega), \tag{8}$$

$$\mathbf{u}^{\mathrm{S}}(\theta,\mathbf{x},\omega)=\omega p_{\mathrm{S}}\mathbf{u}^{\mathrm{S}}(\mathbf{p}=p_{\mathrm{S}}\hat{\mathbf{e}},\mathbf{x},\omega), \tag{9}$$

where $\mathbf{u}^{\mathrm{P}}(\theta,\mathbf{x},\omega)$ and $\mathbf{u}^{\mathrm{S}}(\theta,\mathbf{x},\omega)$ are the local plane P- and S-waves, θ is the propagation direction of local plane waves indicated by the unit vector $\hat{\mathbf{e}}$, $p_{\mathrm{P}}=1/\bar{V}_{\mathrm{P}}$ and $p_{\mathrm{S}}=1/\bar{V}_{\mathrm{S}}$ are the absolute values of P- and S-wave slowness vectors, respectively, and $\bar{V}_{\mathrm{P}}$ and $\bar{V}_{\mathrm{S}}$ are the average P- and S-wave velocities in the sampling window. ωp_{P} and ωp_{S} are the Jacobians of 2D slowness-to-angle tranformation.

As an example, we demonstrate the results of slowness analysis in an elastic model. Shown in Figure 2 is a snapshot of the receiver-side wavefield overlapped on a five-layer velocity model with its parameters listed in Table 1. On the top and bottom of the figure are samples of slowness analyses at the selected locations indicated in the wavefield. For this convergent wavefield, the slowness vectors, i.e., the vectors from the origin of the polar coordinate to these energy peaks, reveal the wave propagation directions and their slowness. At locations simultaneously swept by multiple wavefronts, multiple energy peaks are shown in slowness domain with each peak related to a local plane wave. Following the dispersion relations within the sampling window W, all the P-wave peaks fall on the inner circle with a radius of $1/\bar{V}_{\mathrm{P}}$ and all the S-wave peaks fall on the outer circle with a radius of $1/\bar{V}_{\mathrm{S}}$. With the increase of depth, the radii of these circles become smaller due to the increase of velocities. These results demonstrate that the directional information of P- and S-waves can be fully extracted from their dispersion circles.

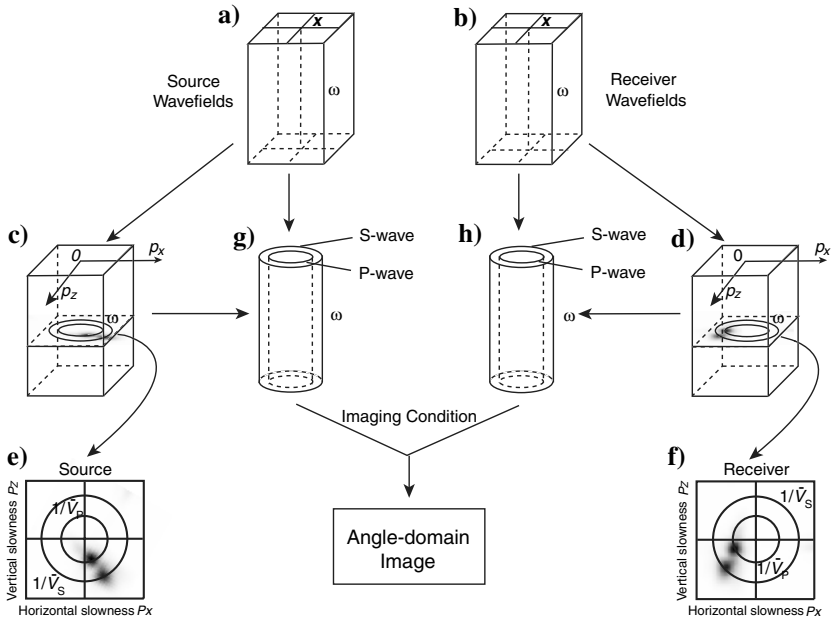

Figure 1. The workflow of slowness analysis. The space-frequency domain source and receiver wavefields (a and b) are transformed to slowness domain data (c and d); (e and f) are cross sections of (c and d) at dominant frequency. Note, in the slowness domain, local plane waves appear as energy peaks fall on the dispersion circles. Thus, the slowness analyses only need to be calculated for cylindrical regions in (g and h). For details, see the text.

ANGLE-DOMAIN IMAGING CONDITION

Similar to the conventional imaging condition, the image for elastic waves can be expressed as the crosscorrelation between the incident (source side) and scattered (receiver side) P- and S-waves, i.e.,

$$I^{\mathrm{PP}}(\mathbf{x}) = \sum_{\omega} u_s^{\mathrm{P}}(\mathbf{x},\omega)[u_g^{\mathrm{P}}(\mathbf{x},\omega)]^*, \tag{10}$$

and

$$I^{\mathrm{PS}}(\mathbf{x}) = \sum_{\omega} u_s^{\mathrm{P}}(\mathbf{x},\omega)[u_g^{\mathrm{S}}(\mathbf{x},\omega)]^*, \tag{11}$$

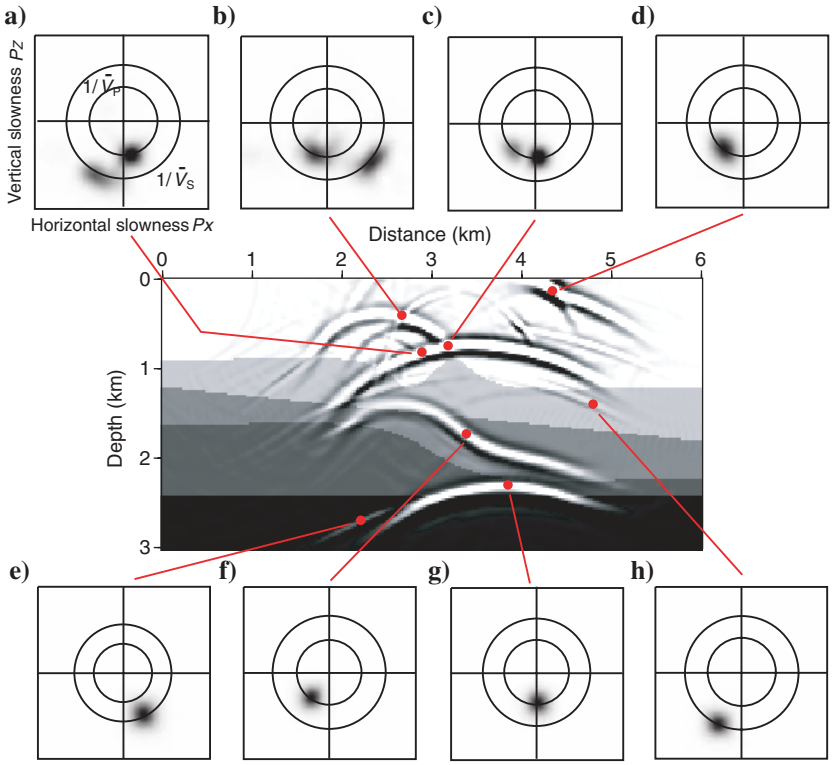

Figure 2. Slowness analyses performed for the receiver-side wavefield in a five-layer model. In the center is the velocity model overlapped by the vertical-component wavefield at $t = T - 0.85s$, where T is the total recording time; (a-h) are slowness domain energy distributions at selected locations indicated in the model.

Table 1. The P- and S-wave velocities and density of the model.

Layer	P-velocity km/s	S-velocity km/s	Density g/cm^3
1	3.50	2.00	2.00
2	3.70	2.12	2.04
3	4.00	2.30	2.10
4	4.20	2.42	2.14
5	4.50	2.60	2.20

where I is the depth image; scalar u is the complex amplitudes of the wavefields; $*$ denotes complex conjugate; superscripts P and S denote the wave types and subscripts s and g denote the source and receiver waves. To obtain the angle-domain imaging condition, we substitute equations 6 and 7 into equations 10 and 11 and obtain

$$I^{\mathrm{PP}}(\mathbf{x}) = \sum_{\theta_s}\sum_{\theta_g} I^{\mathrm{PP}}(\theta_s,\theta_g,\mathbf{x}), \tag{12}$$

and

$$I^{\mathrm{PS}}(\mathbf{x}) = \sum_{\theta_s}\sum_{\theta_g} I^{\mathrm{PS}}(\theta_s,\theta_g,\mathbf{x}), \tag{13}$$

where

$$I^{\mathrm{PP}}(\theta_s,\theta_g,\mathbf{x}) = \sum_{\omega}[\hat{\mathbf{e}}_s^{\mathrm{P}} \cdot \mathbf{u}_s^{\mathrm{P}}(\theta_s,\mathbf{x},\omega)][\hat{\mathbf{e}}_g^{\mathrm{P}} \cdot \mathbf{u}_g^{\mathrm{P}}(\theta_g,\mathbf{x},\omega)]^*, \tag{14}$$

$$I^{PS}(\theta_s,\theta_g,\mathbf{x}) = \sum_{\omega}[\hat{\mathbf{e}}_s^{P} \cdot \mathbf{u}_s^{P}(\theta_s,\mathbf{x},\omega)] \times [\hat{\mathbf{e}}_g^{S} \cdot \mathbf{u}_g^{S}(\theta_g,\mathbf{x},\omega) \cdot \hat{\mathbf{e}}_n]^*, \tag{15}$$

are angle-domain partial images for P-P and P-S scatterings, $\mathbf{u}_s^{\mathrm{P}}$, $\mathbf{u}_g^{\mathrm{P}}$ and $\mathbf{u}_g^{\mathrm{S}}$ are all local plane P- and S-waves. $\hat{\mathbf{e}}_s^{\mathrm{P}}$, $\hat{\mathbf{e}}_g^{\mathrm{P}}$ and $\hat{\mathbf{e}}_g^{\mathrm{S}}$ are unit vectors indicating their propagation directions; θ_s and θ_g are incident and scattering angles, respectively. $\hat{\mathbf{e}}_n$ is the normal vector perpendicular to the propagation plane in which $\hat{\mathbf{e}}_s^{\mathrm{P}}$ and $\hat{\mathbf{e}}_g^{\mathrm{S}}$ are lying.

LOCAL IMAGE MATRIX

At a given image point, we can organize all the partial images in equation 12 or 13, into a matrix according to their incident and scattering angles. This matrix is called "LIM" (e.g., Xie and Wu, 2002; Wu and Chen, 2003). Many important features regarding the velocity models, reflector properties, and acquisition geometry can be revealed by investigating the LIM. We will explore some of these features using numerical examples.

LIM for point scatters

We investigate LIMs for point scatters having perturbations of different elastic parameters. Without losing generality, consider a z-direction P-wave incident on scatters with three different types of perturbations: density ρ, and Lame's constants λ and μ. The interaction of incident wave and perturbation generate scattered waves that are illustrated in Figure 3a to 3c. Different perturbations lead to different radiation patterns that are listed in Table 2 (Wu, 1985). The perturbation $\delta\lambda$ generates only scattered P-wave, whereas the perturbation $\delta\rho$ or $\delta\mu$ generate scattered P- and S-waves. We record scattered P- and S-waves from all directions

and back-propagate them to calculate the LIMs of these scatters. The related P-P LIMs are shown in Figure 3d–3f, and P-S LIMs are shown in Figure 3g–3i. In each LIM, the partial images of these scatters form a common-incident angle strip in LIM at 0° (i.e., the z-direction). The patterns of the image vividly reveal the radiation patterns from different types of perturbations. For a scatter composed of perturbations $\delta\rho$, $\delta\lambda$, and $\delta\mu$, its radiation pattern will be the combination of three basic patterns, and the resultant LIM will be the linear combination of the basic LIMs shown in Figure 3. This will be useful in investigating diffraction points (Zhu and Wu, 2010) or detecting scattering properties of a fractured reservoir (Zheng et al., 2011).

LIM for planar reflectors

A planar reflector can be considered as a line of continuous scatters. The scattered waves from all scatters interfere with each other, forming a reflection wave propagating in a direction dictated by Snell's Law. The sketch in Figure 4a illustrates the process that an incident wave along θ_s generates a scattered wave along θ_g at a locally planar reflector. For convenience, we transfer the acquisition coordinate (θ_s, θ_g) into target coordinate (θ_r, θ_d), where θ_d is the target dipping angle and θ_r is the reflection angle defined as the incident angle relative to the reflector normal.

For the P-P reflection, the coordinate transform can be expressed as (e.g., Xie and Wu, 2002)

$$\theta_d = (\theta_s + \theta_g)/2, \tag{16}$$

and

$$\theta_r = (\theta_s - \theta_g)/2. \tag{17}$$

For the P-S reflection, the coordinate transform is (e.g., Yan and Xie, 2010)

$$\theta_d = \tan^{-1}\frac{\bar{V}_S \sin\theta_s + \bar{V}_P \sin\theta_g}{\bar{V}_S \cos\theta_s + \bar{V}_P \cos\theta_g}, \tag{18}$$

and

$$\theta_r = \theta_s - \theta_d. \tag{19}$$

With these transforms, the LIM can be written as a function of dipping and reflection angles instead of incident and scattering angles. For a reflection event illustrated in Figure 4a, Figure 4b and 4c are their P-P and P-S LIMs, where the horizontal and vertical axes are incident and scattering angles, and the main (from upper left to lower right) and secondary (from upper right to lower left) diagonals are reflection and dipping angle axes. Due to different reflection angles for P- and S-waves, the reflection angle axis in the P-S LIM is curved with the curvature depends on $\bar{V}_P$ to $\bar{V}_S$ ratio. In the P-S LIM, there are two shadow zones in which the incident P-wave and scattered S-wave cannot satisfy Snell's Law.

We use the same five-layer model as used in the previous section to demonstrate the relationship between the local reflector geometries and the energy distributions in the LIMs. Shown in the middle of Figure 5 is the velocity model, in which locations A to D are selected to calculate the LIMs. The model is illuminated by 24 sources and 300 fixed receivers, both covering the entire surface of the model. The LIMs in the top row are for P-P image. At point

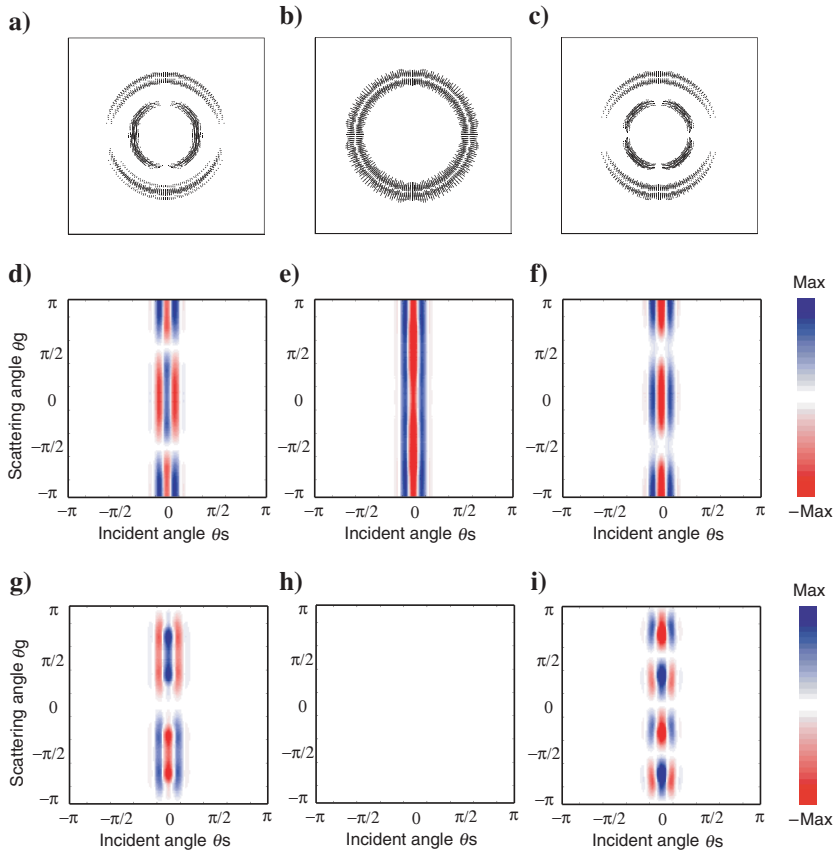

Figure 3. Local image matrices for point scatters with different elastic parameter perturbations, left column: density ρ, middle column: Lame's constant λ, and right column: shear modulus μ; (a-c) are their vectorized displacements of the scattered waves; (d-f) are P-P LIMs, and (g-i) are P-S LIMs.

Table 2. The radiation patterns of scattered P- and S-waves due to perturbations of different elastic parameters.

Perturbations	$\delta\rho$	$\delta\lambda$	$\delta\mu$
P-P scattering	$\cos\theta \cdot \frac{\delta\rho}{\rho_0}$	$-1 \cdot \frac{\delta\lambda}{\lambda_0}$	$-(1+\cos 2\theta) \cdot \frac{\delta\mu}{\mu_0}$
P-S scattering	$\sin\theta \cdot \frac{\delta\rho}{\rho_0}$	$0 \cdot \frac{\delta\lambda}{\lambda_0}$	$\sin 2\theta \cdot \frac{\delta\mu}{\mu_0}$

θ: The scattering angle relative to the incident direction
ρ_0: The background density
λ_0: The background Lame's first parameters
μ_0: The background shear modulus

A, the shape of the reflector is severely away from a planar interface and the image is largely generated by diffracted waves from broad directions. In this context, it is similar to a point scatter. In the related LIM, the energy is distributed over a broad area. Point B is located on a dipping planar interface. To satisfy Snell's Law, the energy is distributed along a strip. Its intersection with the dipping axis gives a dipping angle of approximately 15°, which agrees well with the reflector geometry. The extension of the strip along the reflection axis reveals the illumination coverage at the target. Point C is located on a dipping reflector with slight curvature. The energy distribution in the LIM indicates that the local dip is about 30°. Because of the steep dip angle, the local acquisition aperture is relatively small. Thus, the energy distribution has limited extension along reflection axis and the illumination to this point is relatively poor. Point D is located on a horizontal interface. The energy is distributed at zero dip and, due to located at a great depth, spans a relatively narrow reflection angle compared with that for point B. The bottom row shows LIMs for P-S image. The energy distributions in these LIMs follow the curvature of reflection angle axis. They reveal the same dip information as in P-P LIMs but have slightly different reflection-angle coverage. Note that in P-S LIMs, the P-S conversion is zero at normal incidence, where the sign of images reverses.

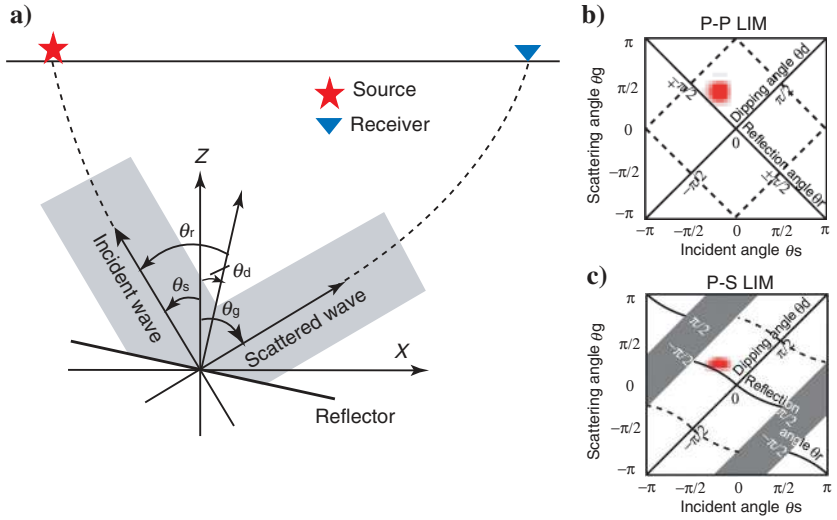

Figure 4. Sketches showing the structure of LIMs: (a) coordinate system used in local angle-domain analysis, where θ_s and θ_g are incident and scattering angles and θ_r and θ_d are reflection and target dipping angles; (b and c) are structures of the P-P and P-S LIMs. Note that the red dots are energy distributions of the related reflection events.

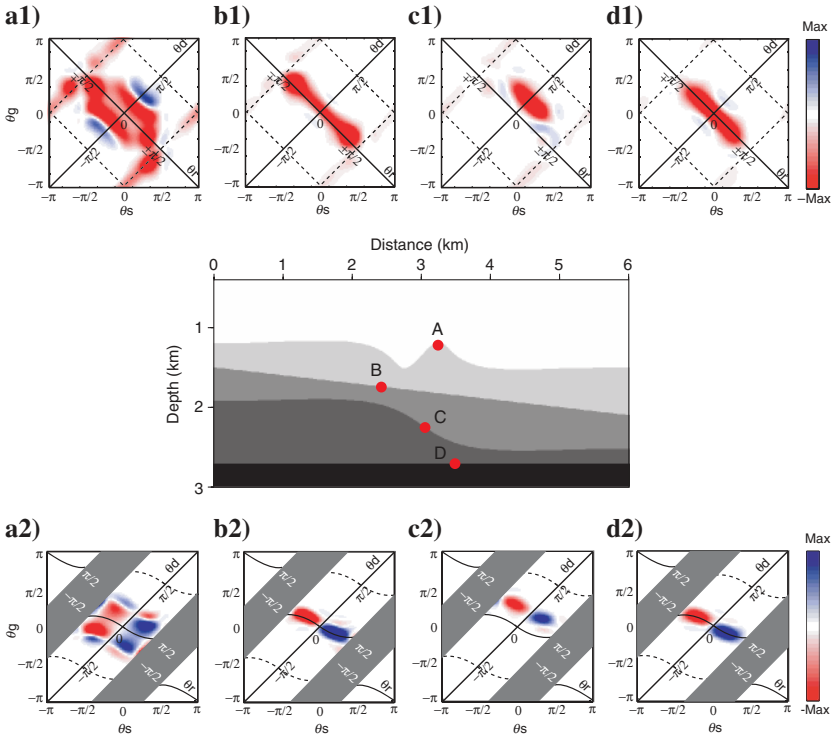

Figure 5. Samples of LIMs at selected locations in a five-layer model. The center is the velocity model, (a1-d1) are P-P LIMs, and (a2-d2) are corresponding P-S LIMs. For coordinate systems in the LIM, refer to Figure 4.

ANGLE-DOMAIN OPERATIONS ON LIM

LIM is expanded from an image pixel with all the related angle information. It is convenient to apply various angle domain operations in the LIM. For example, we can conduct illumination compensation, eliminate unwanted signals, or correct polarization in the LIM (Yan and Xie, 2009, 2010). These operations can be designed highly flexible, e.g., target-oriented, dip-angle-dependent, or reflection-angle-dependent. Here, as examples, we introduce some operations in the LIM to extract angle gathers and to improve the P-P and P-S depth images..

Extracting ADCIG

For a planar reflector, energy is located along a strip in LIM where Snell's Law is satisfied (see, e.g., Figure 5b1–5d1 and 5b2–5d2). Summing up the energy along the common reflection-angle direction will produce the ADCIGs:

$$I^{\mathrm{PP}}(\theta_r, \mathbf{x}) = \sum_{\theta_d} I^{\mathrm{PP}}(\theta_r, \theta_d, \mathbf{x}), \qquad (20)$$

$$I^{\mathrm{PS}}(\theta_r, \mathbf{x}) = \sum_{\theta_d} I^{\mathrm{PS}}(\theta_r, \theta_d, \mathbf{x}). \qquad (21)$$

If the local dip of the reflector can be acquired from some prior information, e.g., from the migrated image, ADCIG can be directly picked from the LIM at θ_d = reflector dip angle.

Eliminating spurious artifacts in P-P image

In Figure 5, some weak energy appears along reflection angles $\pm\pi/2$ for P-P LIM at point A. At this location, beside the true reflections, the forward-propagated and back-propagated head waves meet in phase and spuriously correlate. In a long range, these signals appear as low-wavenumber artifacts in the RTM image. Similar events also are generated by diving waves and back-scattered waves (Yoon et al., 2004). They are particularly serious where high-velocity contrast or gradient exists.

Several methods have been proposed to remove these artifacts, e.g., using different filters at the post image stage (e.g., Youn and Zhou, 2001; Mulder and Plessix, 2004; Guitton et al., 2006), or adopting a nonreflecting wave equation (e.g., Baysal et al., 1983; Fletcher et al., 2005). Another technique is to apply an angle-related weighting function in the imaging condition to eliminate the very wide-angle signals (e.g., Yoon et al., 2004; Xie and Wu, 2006; Liu et al., 2007; Suh and Cai, 2009; Yan and Xie, 2009).

Here, we introduce an angle-domain filter in the LIM to block the very wide-angle energy from entering the image. The resulted angle-domain imaging condition can be expressed as

$$I^{\mathrm{PP}}(\mathbf{x}) = \sum_{\theta_r}\sum_{\theta_d} M^{\mathrm{PP}}(\theta_r,\theta_d) I^{\mathrm{PP}}(\theta_r,\theta_d,\mathbf{x}), \qquad (22)$$

where $M^{\mathrm{PP}}(\theta_r,\theta_d)$ is designed to attenuate events with very wide reflection angles. For example, we can choose to eliminate the energy with reflection angles larger than certain values from the LIM.

Correcting polarity reversal in P-S image

The P-S image usually does not involve artifacts as those that appear in the P-P image. However, polarity reversal occurs because S-wave changes its polarity when crossing the normal incidence (Balch and Erdemir, 1994) (see, e.g., Figure 5a2–5d2). The polarities must be corrected otherwise destructive interference will occur when summing up the partial images into the final image (Lu et al., 2010; Yan and Xie, 2010). Because the polarity of P-S image is controlled by the reflection angles, it is natural to conduct this correction in the LIM. Thus, we apply an angle-domain operator to the P-S partial images

$$I^{\mathrm{PS}}(\mathbf{x}) = \sum_{\theta_r}\sum_{\theta_d} M^{\mathrm{PS}}(\theta_r,\theta_d) I^{\mathrm{PS}}(\theta_r,\theta_d,\mathbf{x}), \qquad (23)$$

where

$$M^{\mathrm{PS}}(\theta_r,\theta_d) = \begin{cases} 1 & \theta_r > 0 \\ 0 & \theta_r = 0 \\ -1 & \theta_r < 0 \end{cases} \qquad (24)$$

is a reflection-angle-dependent operator for correcting the polarity.

NUMERICAL EXAMPLES

We use two examples to demonstrate the calculations of angle gathers and migration images. The first model is the same five-layer model used in the previous section. The synthetic data set is generated using 26 explosion sources and 300 receivers both covering the entire surface of the model. The space between the sources is 0.24 km and the interval between the receivers is 0.024 km. The source time function is a 15-Hz Ricker wavelet. A fourth-order elastic finite difference code is used to extrapolate the source and receiver wavefields. Figures 6, 7, and 8 are P-P and P-S ADCIGs obtained from the true velocity model, and models with +10% and −10% velocity errors. These ADCIGs are calculated at nine horizontal locations from 0.6 to 5.4 km at an interval of 0.6 km and range between −60° and 60°. The polarity of P-S gathers has been corrected. The flat gathers in Figure 6 are from the true velocity model. The gathers that curve down are from the fast model, whereas the gathers that curve up are from the slow model. The actual angular span depends on the effective acquisition aperture and, in general, decreases with the increasing depth. For the sections of reflectors where steep dip angles are involved, the angular span is smaller because of the reduced effective acquisition aperture. Given the acquisition geometry, P-S gathers usually has wider angle coverage compared with the P-P image. Figure 9a and 9b is the correspondent P-P and P-S images after applying the angle-domain operators, i.e., equation 21 and 23, respectively. The two images are quite clean and consistent. Due to its shorter wavelength, the P-S image has higher resolution than the P-P image.

Next, we test our techniques on the Marmousi2 model (Martin et al., 2002). The P- and S-wave velocities and the density are illustrated in Figure 10. The synthetic data set is modeled using 111 surface sources that are located between distances 3.0 and 14.0 km at an interval of 0.1 km. The source time function is a 30-Hz Ricker wavelet. Receivers are located on the seafloor and spaced 0.0125 km apart. For each shot, 361 bilateral receivers are switched on to record the reflection signals. Shown in Figures 11 and 12 are P-P and P-S angle gathers extracted from the data set. These angle gathers are calculated at 17 vertical lines starting from distance 4.5 km with an interval of 0.5 km. The angle range is −68° to 68°. The P-S gathers appear sharper than the P-P gathers because they involve shorter wavelength. Because the correct

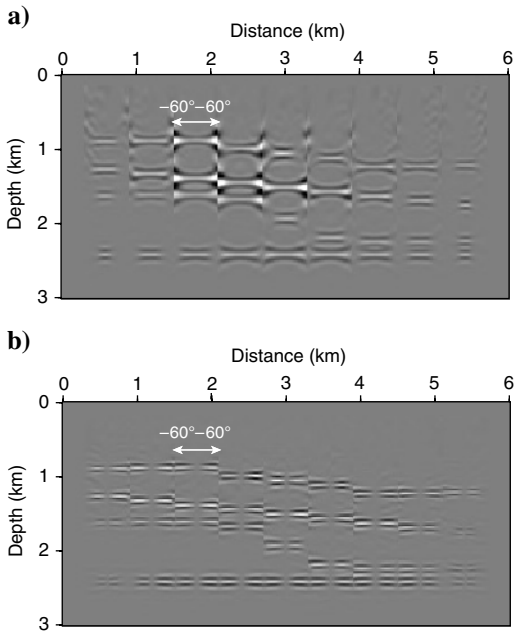

Figure 6. The ADCIGs for (a) P-P and (b) P-S reflections from the true velocity model. The angle range is −60° to 60°.

velocity model is used, the common image gathers generally are flat, except at some steep reflectors where the P-S gathers are a little twisted. Due to limited acquisition aperture and existing velocity gradient, the steep reflectors are mostly illuminated by near normal incident P-waves. Because the P-S conversion is inefficient at small reflection angles, the P-S gathers are usually weaker for steep dip reflectors. Figure 13a and 13b compares the P-P images before and after applying the angle-domain filter. Due to wide angle reflections, the P-P image without angle filter is masked by strong

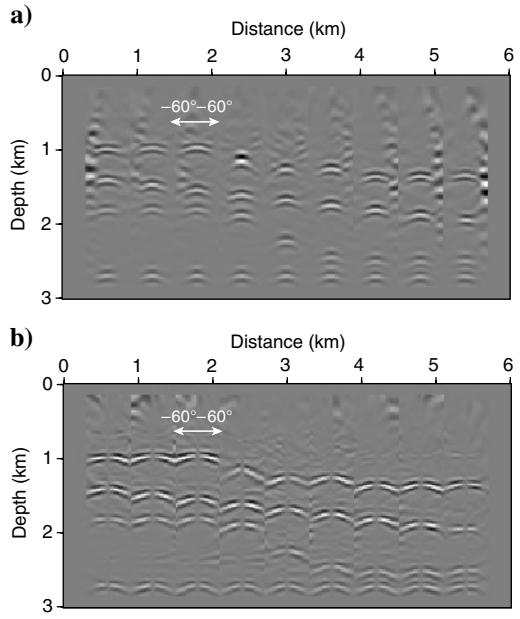

Figure 7. Similar to Figure 6, except the velocity model has +10% errors.

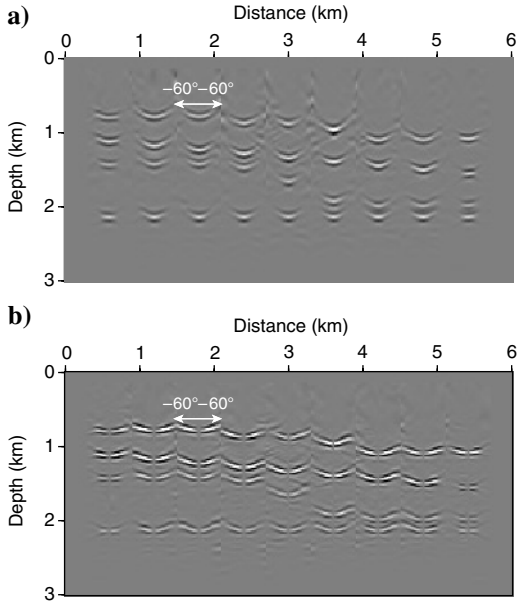

Figure 8. Similar to Figure 6, except the velocity model has −10% errors.

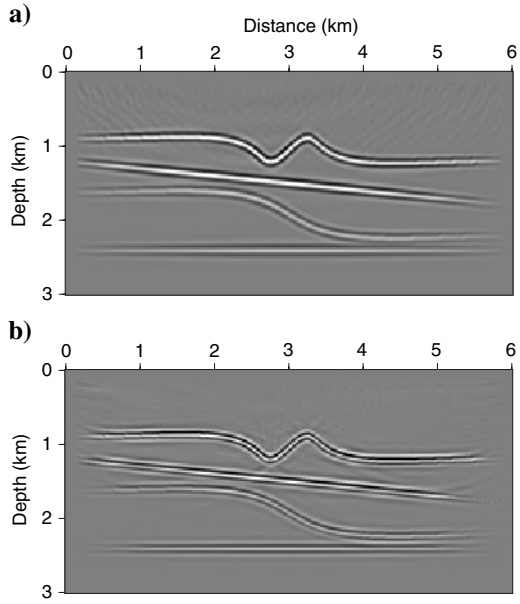

Figure 9. The migration images for the five-layer model, where (a and b) are for P-P and P-S images, respectively. Note that for the P-P image, the wide-angle artifacts have been removed by eliminating the energy with reflection angles larger than 60° from the LIM; and for the P-S image, the polarization reversal has been corrected in the LIM.

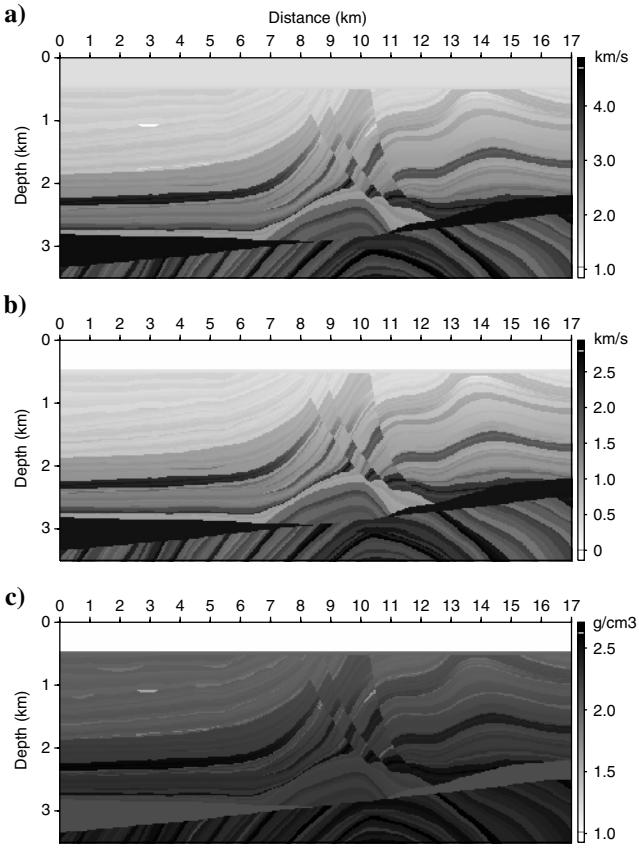

Figure 10. The elastic Marmousi2 model, with (a) P-wave velocity, (b) S-wave velocity, and (c) density.

artifacts, especially at the shallow regions. With the angle-domain imaging condition, the artifacts effectively are removed, whereas the images of the interfaces are well kept. Shown in Figure 14a is the P-S image without applying the angle-domain operator, where some partial images from different shots cancel each other out, causing the blurring of the image. After polarization correction, the image in Figure 14b greatly is enhanced.

DISCUSSIONS

To extract the angle-related information from the wavefield, integral method (e.g., slant stack or windowed FFT) and differential method (e.g., calculate the Poynting vector or displacement vector) can be used. The former is more stable but relatively time-consuming and the latter is more efficient but may lead to unstable results in a complicated wavefield. For example, in a complex velocity model, multiple wavefronts may simultaneously arrive at a given location from various directions. The differential method may give an ambiguous result, due to its incapability to identify multiple propagation directions.

To properly conduct angle decomposition, choosing correct window size, shape, and sampling rate are crucial. According to uncertainty principle, there is always a trade-off between the space and angle resolution. A larger sampling window improves the angle accuracy but makes the result less localized in space, and vice versa. We choose the window size that is one to two wavelengths at the dominant frequency. Within this range, a complex wavefront can be decomposed into a superposition of local plane waves and their propagation directions can be extracted properly. Different window

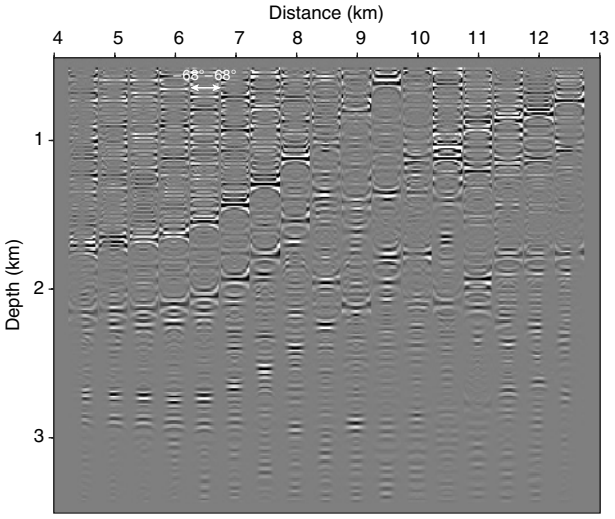

Figure 11. The P-P ADCIGs extracted from Marmousi2 model. The angle range is −68° to 68°.

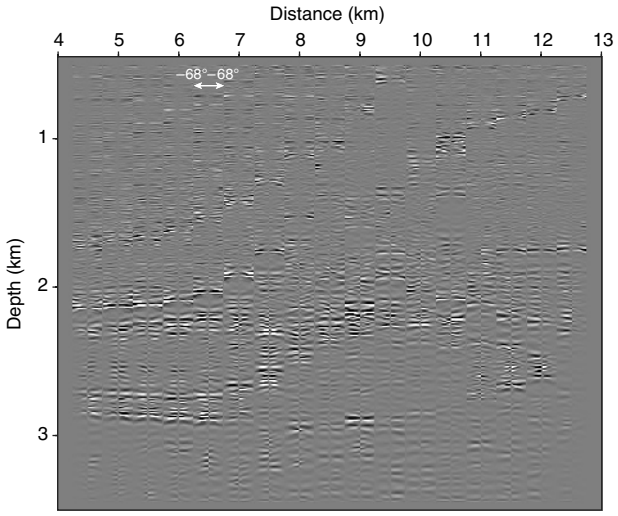

Figure 12. Similar to Figure 11, except for the P-S image.

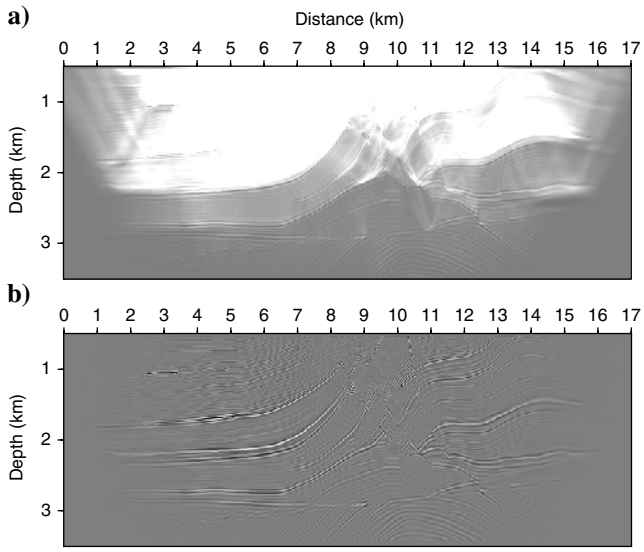

Figure 13. Comparison of migrated P-P images for Marmousi2 model, where (a) is the image before applying the angle-domain operator, and (b) is the image where reflections with angle larger than 68° have been eliminated.

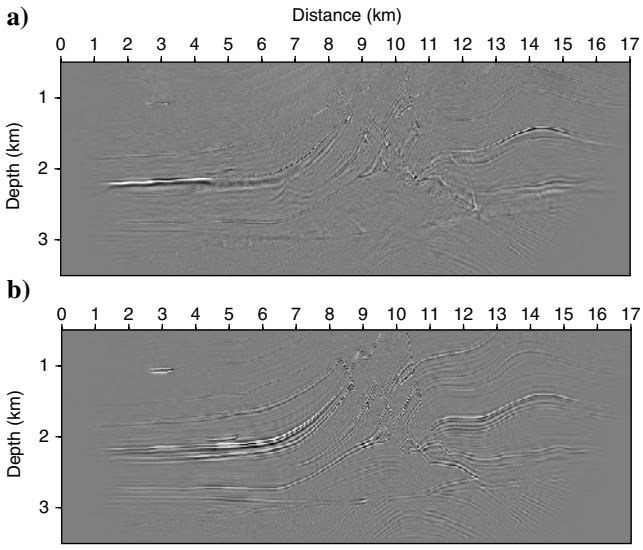

Figure 14. Similar to Figure 13, except it is for P-S image. Note that in (b), the polarization reversal has been corrected from the LIM.

sizes are used for P- and S-modes due to their different wavelengths. To avoid the numerical aliasing caused by coarse sampling, we choose a sampling rate about twice per minimum wavelength. In all the examples presented here, we use simple rectangular windows. Though quite simple, it yields better angle resolution compared with window functions with edge tapers, such as the Gaussian window.

We compare the efficiency of our method with conventional local slant stack and windowed FFT method. Conventional local slant stacking is implemented in the entire slowness/wavenumber space. The slant stack along the dispersion circles can save tremendous computations and it is usually one to two orders of magnitude faster. In addition, the proposed method directly generates angle components while windowed FFT outputs wavenumber components, followed by a conversion from wavenumber to angle. To output finely sampled angle components, zero padding around the spatial window is usually required by the windowed FFT but not required by the local slant stack. Even though FFT is a fast algorithm, it will raise considerably the computational cost to enlarge the window size. On the other hand, it will lower the efficiency of our method to increase the number of directions, but will not affect the windowed FFT method. In general, the efficiencies of the local slant stack along the dispersion circle and the windowed FFT methods are comparable and are dependent on the detailed treatments. Zhang et al. (2010) and Xu et al. (2011) extensively discussed methods to improve the efficiency of the windowed FFT method.

CONCLUSIONS

For elastic RTM, we present a slowness-based method to decompose the P- and S-waves into angle components and formulate the angle-domain partial image as the crosscorrelation of the decomposed local plane waves. Collecting all the angle-domain partial images, we construct the LIMs for P-P and P-S images. LIM is a convenient tool for investigating the angle-related problems in wave propagation and imaging. Sorting the energy in LIM can generate different ADCIGs that can be used for velocity, amplitude, and illumination analyses. The target is not necessarily locally planar as required by other methods. For point scatters, their radiation patterns in the LIM are related to the material properties of elastic perturbations. For a locally planar reflector, the incident and scattered waves are controlled by Snell's Law. In the P-P LIM, the energy forms a strip, and for the P-S image the energy forms a curved strip because reflection angles are different for incident and scattered waves. Summing up energy in the LIM produces the depth image. Angle-related operations, e.g., eliminating the unwanted artifacts, correcting for acquisition aperture effect or polarization effect, can be conveniently performed in LIM and lead to ADCIGs or migration images with improved quality. To validate our method, P-P and P-S angle gathers and images are computed for the synthetic data sets generated from a five-layer elastic model and the elastic Marmousi2 model. The current technique can be extended to 3D isotropic and anisotropic cases.

ACKNOWLEDGMENTS

We thank the associate editor Sheng Xu, Yanghua Wang, and two anonymous reviewers for their valuable comments that greatly improved this manuscript. This research is supported by the WTOPI Consortium at the University of California, Santa Cruz.

REFERENCES

Aki, K., and P. G. Richards, 1980, Quantitative seismology: Theory and methods: W. H. Freeman and Co.

Balch, A., and C. Erdemir, 1994, Sign-change correction for prestack migration of P-S converted wave reflections: Geophysical Prospecting, **42**, 637–663, doi: 10.1111/gpr.1994.42.issue-6.

Baysal, E., D. D. Kosloff, and J. W. C. Sherwood, 1983, Reverse-time migration: Geophysics, **48**, 1514–1524, doi: 10.1190/1.1441434.

Biondi, B., and W. Symes, 2004, Angle-domain common-image gathers for migration velocity analysis by wavefield continuation imaging: Geophysics, **69**, 1283–1298, doi: 10.1190/1.1801945.

Brandsberg-Dahl, S., M. V. De Hoop, and B. Ursin, 2003, Focusing in dip and AVA compensation on scattering-angle/azimuth common-image gathers: Geophysics, **68**, 232–254, doi: 10.1190/1.1543210.

Cao, J., and R. S. Wu, 2009a, Fast acquisition aperture correction in prestack depth migration using beamlet decomposition: Geophysics, **74**, no. 4, S67–S74, doi: 10.1190/1.3116284.

Cao, J., and R. S. Wu, 2009b, Full-wave directional illumination analysis in the frequency domain: Geophysics, **74**, no. 4, S85–S93, doi: 10.1190/1.3131383.

Chang, W. F., and G. A. McMechan, 1987, Elastic reverse-time migration: Geophysics, **52**, 1365–1375, doi: 10.1190/1.1442249.

Chang, W. F., and G. A. McMechan, 1994, 3D elastic prestack, reverse-time depth migration: Geophysics, **59**, 597–609, doi: 10.1190/1.1443620.

Chen, L., R. S. Wu, and Y. Chen, 2006, Target-oriented beamlet migration based on Gabor-Daubechies frame decomposition: Geophysics, **71**, no. 2, S37–S52, doi: 10.1190/1.2187781.

Claerbout, J. F., 1985, Imaging the earth's interior: Blackwell Scientific Publications.

Dai, T. F., and J. T. Kuo, 1986, Real data results of Kirchhoff elastic wave migration: Geophysics, **51**, 1006–1011, doi: 10.1190/1.1442139.

Dellinger, J., and J. Etgen, 1990, Wavefield separation in two-dimensional anisotropic media: Geophysics, **55**, 914–919, doi: 10.1190/1.1442906.

Dickens, A., and G. A. Winbow, 2011, RTM angle gathers using Poynting vectors: 81st Annual International Meeting, SEG, Expanded Abstracts, 3109–3113, doi: 10.1190/1.3627841.

Fletcher, R. P., P. J. Fowler, and P. Kitchenside, 2005, Suppressing artifacts in prestack reverse-time migration: 75th Annual International Meeting, SEG, Expanded Abstracts, 2049–2051.

Guitton, A., B. Kaelin, and B. Biondi, 2006, Least-square attenuation of reverse-time migration artifacts: 76th Annual International Meeting, SEG, Expanded Abstracts, 2348–2352.

Hokstad, K., 2000, Multicomponent Kirchhoff migration: Geophysics, **65**, 861–873, doi: 10.1190/1.1444783.

Hou, A., and K. Marfurt, 2002, Multicomponent prestack depth migration by scalar wavefield extrapolation: Geophysics, **67**, 1886–1894, doi: 10.1190/1.1527088.

Jin, S. W., C. C. Mosher, and R. S. Wu, 2002, Offset-domain pseudoscreen prestack depth migration: Geophysics, **67**, 1895–1902, doi: 10.1190/1.1527089.

Kuo, J. T., and T. F. Dai, 1984, Kirchhoff elastic wave migration for the case of noncoincident source and receiver: Geophysics, **49**, 1223–1238, doi: 10.1190/1.1441751.

Liu, F., G. Zhang, S. A. Morton, and J. P. Leveille, 2007, Reverse-time migration using one-way wavefield imaging condition: 77th Annual International Meeting, SEG, Expanded Abstracts, 2170–2174.

Lu, R., P. Traynin, and J. E. Anderson, 2009, Comparison of elastic and acoustic reverse-time migration on the synthetic elastic Marmousi-II OBC data set: 79th Annual International Meeting, SEG, Expanded Abstracts, **28**, 2799–2803.

Lu, R., J. Yan, J. E. Anderson, and T. Dickens, 2010, Elastic RTM: Anisotropic wave-mode separation and converted-wave polarization correction: 80th Annual International Meeting, SEG, Expanded Abstracts, 3171–3175.

Luo, M. Q., J. Cao, X. B. Xie, and R. S. Wu, 2004, Comparison of illumination analysis using one-way and full-wave propagators: 74th Annual International Meeting, SEG, Expanded Abstracts, 67–70.

Mao, J., R. S. Wu, and J. H. Gao, 2010, Directional illumination analysis using the local exponential beamlet: Geophysics, **75**, no. 4, S163–S174, doi: 10.1190/1.3454361.

Martin, G. S., K. J. Marfurt, and S. Larsen, 2002, Marmousi-2: An updated model for the investigation of AVO in structurally complex areas: 72nd Annual International Meeting, SEG, Expanded Abstracts, 1979–1982.

Mosher, C. C., and D. J. Foster, 2000, Common-angle imaging conditions for prestack depth migration: 70th Annual International Meeting, SEG, Expanded Abstracts, 830–833.

Mosher, C. C., D. J. Foster, and S. Hassanzadeh, 1997, Common angle imaging with offset plane waves: 67th Annual International Meeting, SEG, Expanded Abstracts, 1379–1382.

Mulder, W. A., and R. E. Plessix, 2004, A comparison between one-way and two-way wave-equation migration: Geophysics, **69**, 1491–1504, doi: 10.1190/1.1836822.

Prucha, M., B. Biondi, and W. Symes, 1999, Angle-domain common-image gathers by wave-equation migration: 69th Annual International Meeting, SEG, Expanded Abstracts, 824–827.

Rickett, J. E., and P. C. Sava, 2002, Offset and angle-domain common image-point gathers for shot-profile migration: Geophysics, **67**, 883–889, doi: 10.1190/1.1484531.

Sava, P., and S. Fomel, 2003, Angle-domain common image gathers by wavefield continuation methods: Geophysics, **68**, 1065–1074, doi: 10.1190/1.1581078.

Sava, P., and S. Fomel, 2005a, Coordinate-independent angle-gathers for wave equation migration: 75th Annual International Meeting, SEG, Expanded Abstracts, 2052–2055.

Sava, P., and S. Fomel, 2005b, Time-shift imaging condition: 75th Annual International Meeting, SEG, Expanded Abstracts, 1850–1853.

Sava, P., and S. Fomel, 2005c, Wave-equation common angle gathers for converted waves: 75th Annual International Meeting, SEG, Expanded Abstracts, 947–950.

Sava, P., and I. Vasconcelos, 2011, Extended imaging condition for wave-equation migration: Geophysical Prospecting, **59**, 35–55, doi: 10.1111/gpr.2010.59.issue-1.

Sava, P., and I. Vlad, 2011, Wide-azimuth angle gathers for wave-equation migration: Geophysics, **76**, no. 3, S131–S141, doi: 10.1190/1.3560519.

Soubaras, R., 2003, Angle gathers for shot-record migration by local harmonic decomposition: 73rd Annual International Meeting, SEG, Expanded Abstracts, 889–892.

Suh, S. Y., and J. Cai, 2009, Reverse-time migration by fan filtering plus wavefield decomposition: 79th Annual International Meeting, SEG, Expanded Abstracts, 2804–2807.

Sun, R., J. Chow, and K. J. Chen, 2001, Phase correction in separating P- and S-waves in elastic data: Geophysics, **66**, 1515–1518, doi: 10.1190/1.1487097.

Sun, R., and G. A. McMechan, 1986, Prestack reverse-time migration for elastic waves with application to synthetic offset vertical seismic profiles: Proceedings of the IEEE, **74**, 457–465, doi: 10.1109/PROC.1986.13486.

Sun, R., and G. A. McMechan, 2001, Scalar reverse-time depth migration of prestack elastic seismic data: Geophysics, **66**, 1519–1527, doi: 10.1190/1.1487098.

Wu, R. S., and K. Aki, 1985, Scattering characteristics of elastic waves by an elastic heterogeneity: Geophysics, **50**, 582–595, doi: 10.1190/1.1441934.

Wu, R. S., and L. Chen, 2002, Mapping directional illumination and acquisition aperture efficacy by beamlet propagators: 72nd Annual International Meeting, SEG, Expanded Abstracts, 1352–1355.

Wu, R. S., and L. Chen, 2003, Prestack depth migration in angle-domain using beamlet decomposition: Local image matrix and local AVA: 73rd Annual International Meeting, SEG, Expanded Abstracts, 973–976.

Wu, R. S., and L. Chen, 2006, Directional illumination analysis using beamlet decomposition and propagation: Geophysics, **71**, no. 4, S147–S159, doi: 10.1190/1.2204963.

Wu, R. S., L. Chen, and X. B. Xie, 2003, Directional illumination and acquisition dip-response: 65th Annual International Conference and Exhibition, EAGE, Extended Abstracts, P147.

Wu, R. S., and J. Mao, 2007, Beamlet migration using local harmonic bases: 77th Annual International Meeting, SEG, Expanded Abstracts, 2230–2234.

Wu, R. S., Y. Wang, and M. Luo, 2008, Beamlet migration using local cosine basis: Geophysics, **73**, no. 5, S207–S217, doi: 10.1190/1.2969776.

Wu, R. S., X. B. Xie, M. Fehler, and L. J. Huang, 2006, Resolution analysis of seismic imaging: 68th Annual International Conference and Exhibition, EAGE, Extended Abstracts, G048.

Xie, X. B., Z. Ge, and T. Lay, 2005a, Investigating explosion source energy partitioning and Lg-wave excitation using a finite-difference plus slowness analysis method: Bulletin of the Seismological Society of America, **95**, 2412–2427, doi: 10.1785/0120050023.

Xie, X. B., S. W. Jin, and R. S. Wu, 2006, Wave-equation-based seismic illumination analysis: Geophysics, **71**, no. 5, S169–S177, doi: 10.1190/1.2227619.

Xie, X. B., and T. Lay, 1994, The excitation of explosion Lg, a finite-difference investigation: Bulletin of the Seismological Society of America. **84**, 324–342.

Xie, X. B., and R. S. Wu, 2002, Extracting angle domain information from migrated wavefields: 72nd Annual International Meeting, SEG, Expanded Abstracts, 1360–1363.

Xie, X. B., and R. S. Wu, 2005, Multicomponent prestack depth migration using elastic screen method: Geophysics, **70**, no. 1, S30–S37, doi: 10.1190/1.1852787.

Xie, X. B., and R. S. Wu, 2006, A depth migration method based on the full-wave reverse-time calculation and local one-way propagation: 76th Annual International Meeting, SEG, Expanded Abstracts, 2333–2337.

Xie, X. B., R. S. Wu, M. Fehler, and L. Huang, 2005b, A wave-equation-based analysis: Seismic resolution and illumination: 75th Annual International Meeting, SEG, Expanded Abstracts, 1862–1865.

Xie, X. B., and H. Yang, 2008, A full-wave equation based seismic illumination analysis methods: 70th Annual International Conference and Exhibition, EAGE, Extended Abstracts, P284.

Xu, S., H. Chauris, G. Lambare, and M. Noble, 2001, Common-angle migration: A strategy for imaging complex media: Geophysics, **66**, 1877–1894, doi: 10.1190/1.1487131.

Xu, S., Y. Zhang, and B. Tang, 2011, 3D common-image gathers from reverse time migration: Geophysics, **76**, no. 2, S77–S92, doi: 10.1190/1.3536527.

Yan, J., and P. Sava, 2008, Isotropic angle-domain elastic reverse-time migration: Geophysics, **73**, no. 6, S229–S239, doi: 10.1190/1.2981241.

Yan, R., and X. B. Xie, 2009, A new angle-domain imaging condition for reverse time migration: 79th Annual International Meeting, SEG, Expanded Abstracts, 2784–2788.

Yan, R., and X. B. Xie, 2010, A new angle-domain imaging condition for elastic reverse time migration: 80th Annual International Meeting, SEG, Expanded Abstracts, 3181–3186.

Yoon, K., M. Guo, J. Cai, and B. Wang, 2011, 3D RTM angle gathers from source wave propagation direction and dip of reflector: 81st Annual International Meeting, SEG, Expanded Abstracts, 3136–3139.

Yoon, K., K. Marfurt, and E. W. Starr, 2004, Challenges in reverse-time migration: 74th Annual International Meeting, SEG, Expanded Abstracts, 1057–1060.

Youn, O., and H. W. Zhou, 2001, Depth imaging with multiples: Geophysics, **66**, 246–255, doi: 10.1190/1.1444901.

Zhang, Q., and G. A. McMechan, 2010, 2D and 3D elastic wavefield vector decomposition in the wavenumber-domain for VTI media: Geophysics, **75**, no. 3, D13–D26, doi: 10.1190/1.3431045.

Zhang, Q., and G. A. McMechan, 2011a, Direct vector-field method to obtain angle-domain common-image gathers for isotropic acoustic and elastic reverse-time migration: Geophysics, **76**, no. 5, WB135–WB149, doi: 10.1190/geo2010-0314.1.

Zhang, Q., and G. A. McMechan, 2011b, Common-image gathers in the incident phase-angle domain from reverse-time migration in 2D elastic VTI media: Geophysics, **76**, no. 6, S197–S206, doi: 10.1190/geo2011-0015.1.

Zhang, Y., S. Xu, B. Tang, B. Bai, Y. Huang, and T. Huang, 2010, Angle gathers from reverse-time migration: The Leading Edge, **29**, 1364–1371, doi: 10.1190/1.3517308.

Zhe, J., and S. A. Greenhalgh, 1997, Prestack multicomponent migration: Geophysics, **62**, 598–613, doi: 10.1190/1.1444169.

Zheng, Y., X. Fang, M. Fehler, and D. Burns, 2011, Double-beam stacking to infer seismic properties of fractured reservoirs: 81st Annual International Meeting, SEG, Expanded Abstracts, 1809–1813.

Zhu, X., and R. S. Wu, 2010, Imaging diffraction points using the local image matrices generated in prestack migration: Geophysics, **75**, no. 1, S1–S9, doi: 10.1190/1.3277252.